

# Investigations on New Electrolyte Composition and Modified Membrane for High Voltage Zinc–Manganese Hybrid Redox Flow Batteries

Raghu pandiyan Naresh,<sup>[a, b]</sup> K. Mariyappan,<sup>[a, b]</sup> Ditty Dixon,<sup>[a, b]</sup> M. Ulaganathan,\*<sup>[a, b]</sup> and P. Ragupathy\*<sup>[a, b]</sup>

In this work, the effect of electrolyte composition and the pore filled membrane was investigated in zinc–manganese (Zn–Mn) hybrid redox flow battery (HRFB). Among the studied electrolytes compositions, sulfate-based electrolyte composition exhibits an improved performance at various conditions. Further, to minimize the ion crossover, the Daramic membrane is modified using polyacrylonitrile (PAN) as a pore filling agent. Hence, the flow cell fabricated with the optimized electrolyte and modified membrane enhanced the overall cell performance, particularly the energy efficiency of 75.45% was achieved for the optimized conditions. As configured Zn–Mn flow cell system showed high

avg. discharge plateau of 1.91 V at 10 mA cm<sup>-2</sup>. Further, the cell employed the modified membrane experienced the highly improved performance up to 40 mA cm<sup>-2</sup>. Besides that, the durability of the Zn–Mn system employing PAN filled Daramic membrane revealed the consistent cell performance over 100 galvanostatic charge-discharge (GCD) cycles. Thus, the proposed sulfate-based precursors electrolyte combinations and PAN filled Daramic membrane can be considered as a proficient candidate for obtaining better performance Zn–Mn flow cell system.

## 1. Introduction

Fulfilling the energy demand with the development of high performance, cost-effective, eco-friendly, and high voltage energy storage devices around the world is enormously increased.<sup>[1]</sup> Over the decades, energy crises have been increased drastically worldwide due to the extinction of nature-based fossil fuels in the earth's crust.<sup>[2]</sup> This leads to the utilization of alternative natural energy resources such as wind, hydro and solar for generating the electricity; however, due to the environmental calamity and intermittent nature of the above renewable sources, it is difficult to fully convert as the electrical energy and connecting with the grids directly for fulfilling the energy requirement. Moreover, the direct connection of such energy conversion to the grid connectivity causes severe power loss which is about nearly 30%. To avoid such losses and utilizing the harvesting power during the peak hours, highly suitable high energy storage devices becomes essential. Therefore, storing of electrical energy in a large scale has been emerged as a significant requirement. The electro-

chemical energy storage (EES) technologies might be a proficient candidature with various appealing characteristics such as long cycling, high energy density, fast charge, and high reliability. Hence the EES technologies would be a better option for fulfilling the energy demand. At present, several energy storage devices have been developed and commercialized including Li-ion battery,<sup>[3–4]</sup> Lead acid battery,<sup>[5]</sup> redox flow batteries.<sup>[6–7]</sup> Among these, Li-ion batteries are the most matured system and widely using in portable devices and electric vehicles. However, the high cost of lithium, low abundance, and safety obstructs their application in large scale energy storage. Hence, alternatives to Li-ion batteries are urgently required to meet the energy demand of large scale energy storage applications, particularly for stationary storage applications. For the past few decades, redox flow batteries have gained attention for large scale energy storage applications and commercialized successfully.<sup>[8–11]</sup> The peculiar characteristic behaviors of redox flow batteries are decoupling of energy and power, depth of discharge, long cycle life, scalable, low self-discharge, high energy density, and high power density. In a redox flow battery, the redox-active species are dissolved in a suitable solvent to get appropriate concentrations, which were constantly circulated, into the cell using an external pump. The all metal-based flow battery has more benefits over the other flow batteries due to long cycle life, high energy density, and high cell voltage. There are numerous all metal-based flow battery has been developed over the past few decades based on the redox couple involved in the cell reaction such as Zn–Br<sub>2</sub>,<sup>[12–14]</sup> all vanadium redox flow battery (VRFB),<sup>[15]</sup> Zn-polyiodide,<sup>[16]</sup> Fe–Cr,<sup>[17]</sup> Fe–V,<sup>[18]</sup> Fe–Mn,<sup>[19]</sup> Zn–V<sup>[20]</sup> and Zn–Fe.<sup>[21]</sup> Among these, all vanadium and Zn–Br<sub>2</sub> systems are successfully commercialized. However, all vanadium possess

[a] R. p. Naresh, K. Mariyappan, Dr. D. Dixon, Dr. M. Ulaganathan, Dr. P. Ragupathy  
Electrochemical Power Sources Division  
CSIR-Central Electrochemical Research Institute (CECRI)  
630003 Karaikudi, Tamil Nadu, India  
E-mail: mulaganathan@cecri.res.in  
ragupathyp@cecri.res.in

[b] R. p. Naresh, K. Mariyappan, Dr. D. Dixon, Dr. M. Ulaganathan, Dr. P. Ragupathy  
Academy of Scientific and Innovative Research (AcSIR)  
201002 Ghaziabad, India

 Supporting information for this article is available on the WWW under  
<https://doi.org/10.1002/batt.202100071>

serious limitations such as low energy density (20–25 Wh L<sup>-1</sup>) and the use of expensive Nafion-117 membrane which increases the overall cost of the system.<sup>[22]</sup> In the case of Zn–Br<sub>2</sub> flow battery, the formation of elemental bromine and zinc dendritic growth during the charging process are the critical issues limiting the performance of the flow cells. The corrosive behavior of elemental bromine affects the cell components severely, this can be minimized by adding quaternary ammonium based ionic liquids which can encapsulate the elemental bromine and forms a polybromide complex which reduces the vapor pressure of the solution. The formation of a polybromide complex separates out from the aqueous solution and forms an oily dense liquid which settles down in the tank and subsequently limits the cell performance.<sup>[19–22]</sup> On the other hand, the expensive nature of the complexing agents and poor cycle life forced to find an alternate system where the system should be less expensive, chemically stable, and more eco-friendly. At the same time, Zn based hybrid redox couples are quite attractive than any other redox couples due to their fast kinetics of zinc with negative potential of ( $E^{\circ} = -0.76$  V vs SHE).<sup>[23]</sup> However, the selection of positive redox couple is very crucial to attain high voltage and reversibility of the system. In recent years, there are several reports focused on Zn based hybrid flow battery systems where various redox pairs have been used in the positive side, among them Br<sup>-</sup>/Br<sub>2</sub>, Ce<sup>3+</sup>/Ce<sup>4+</sup> and V<sup>4+</sup>/V<sup>5+</sup> and polyiodide were studied extensively.<sup>[24–26]</sup> However, it has its own limitations such as poor reversibility, poor solubility and fade electrochemical activity.

Recently, manganese-based redox electrolytes have been received much attention due to the high solubility, ease of preparation, eco-friendly, and good reversibility in aqueous electrolytes, and more importantly the existence of multiple oxidation states from +2 to +7 with high positive reduction potential.<sup>[27–31]</sup> The standard electrode potentials of the efficient positive redox couples are still lower than Mn<sup>2+</sup>/Mn<sup>3+</sup> redox species (1.51 V vs SHE). The high standard electrode potential of Mn<sup>2+</sup>/Mn<sup>3+</sup> will eventually increase the cell voltage of the system when combined with negative redox species. Therefore, the Mn<sup>2+</sup>/Mn<sup>3+</sup> redox couple has been more attracted and well adopted as a catholyte for flow battery applications. Moreover, the stability of Mn<sup>3+</sup> is very low in an aqueous medium which is then instantaneously converted into manganese dioxide (MnO<sub>2</sub>). The as-formed MnO<sub>2</sub> gets deposited on the positive electrode during the charging process. The deposited MnO<sub>2</sub> severely affects the areal capacity and electrolyte flow in the cell which hampered the performance of the flow cell. Exhaustive research is still required to address the listed challenges in the Mn<sup>2+</sup>/Mn<sup>3+</sup> redox couple to get better performance in RFBs. This provides more insights to develop novel electrode materials and electrolyte additives to enhance the flow cell performance by proficiently suppressing the formation of MnO<sub>2</sub>. Moreover, one way of suppressing the formation of MnO<sub>2</sub> is use the electrolyte in a slightly acidic environment. A recent study demonstrated the manganese redox couple in a Zn–Mn HFRB where the manganese is dissolved in methane sulfonic acid (MSA) as a supporting electrolyte which shows 74% energy and 92.25% coulombic

efficiency at a current density of 20 mA cm<sup>-2</sup> for ten cycles. The presence of MSA stabilizes the Mn<sup>3+</sup> species in the electrolyte as a result it enhances the electrochemical kinetics of Mn<sup>2+</sup>/Mn<sup>3+</sup> redox couple. The Mn<sup>3+</sup> species is more stable when the concentration of MSA is increased from 2 to 5 M.<sup>[29]</sup> The electrode materials significantly determine the performance of the Mn<sup>2+</sup>/Mn<sup>3+</sup> redox couple. The fabrication of highly conductive and high surface area materials to electrode eventually enhance the kinetics of Mn<sup>2+</sup>/Mn<sup>3+</sup> redox couple.<sup>[30]</sup> Apart from Zn–Mn redox couples, various manganese based redox pairs such as Mn–Ti,<sup>[31]</sup> Mn–V,<sup>[32]</sup> Mn–Cu,<sup>[33]</sup> and Mn–H<sup>[34]</sup> have been proposed in the last few decades. Though the manganese based redox couples fascinates towards electrical energy storage they still possess some intrinsic limitations when it couples with anolyte. In Mn–Ti system, the greater hydrolysis tendency of titanium results the degradation in cycling performance. The use of vanadium ions in Mn–V flow cell leads to severe crossover contaminations which subsequently reduce the coulombic efficiency of the flow cell. The practical usage of the Mn–H system is highly challenging because of hydrogen storage and the need of novel electrocatalyst which eventually increases the capital cost of the system. This hinders the successful development of the Mn–H flow battery systems in real time applications. The utilization of copper as anolyte in Mn–Cu flow systems leads to dendrite growth at the anode while operating the system at a higher current density. Hence, choosing of best redox couple has been a critical task and urgently required to improve the performance of the manganese-based flow battery system.<sup>[35]</sup> The aqueous Zn–Mn is the best redox couple for scalable sustainable energy storage applications. The basic electrochemical reactions which occur during the cell operation at both anode and cathode in the given Zn–Mn HFRB are described as below:

At the negative electrode [Eq. (1)]:



At the positive electrode [Eq. (2)]:



Net cell reaction [Eq. (3)]:



During the charging process, the Zn<sup>2+</sup> ions get reduced to metallic Zn and get deposited on the surface of the electrode in the anode whereas, at the cathode, Mn<sup>2+</sup> is oxidized to form Mn<sup>3+</sup> which is unstable in aqueous medium and suddenly disproportionate into MnO<sub>2</sub> which deposits on the surface of the electrode in the cathode. During the discharge process, the reverse reaction occurs, and vice versa.<sup>[36]</sup>

In the present work, we have successfully developed new electrolyte composition for obtaining the better performance

of zinc manganese (Zn–Mn) hybrid redox flow battery (HRFB). Interestingly, the aqueous Zn–Mn hybrid redox flow battery exhibits an extremely high discharge voltage of 1.91 V when sulfate-based precursors had been used. However, still severe crossover of the electrolyte was observed. Here, the crossover effect was minimized by using pore filled Daramic membrane where polyacrylonitrile (PAN) dissolved in N-Methyl-Pyrrolidone (NMP) was used as a porous filling agent. Thus, the GCD curves of the flow cell were also recorded up to a maximum current density of  $40 \text{ mA cm}^{-2}$  with uninterrupted cell performance. The aqueous sulfate-based Zn–Mn system with PAN coated Daramic membrane is considered to be the significant module for high energy storage with low cost and environmentally benign systems.

## Experimental Section

### Materials and Electrolyte Preparation

The chemicals used in this study include Manganese sulfate monohydrate (99%, SRL Pvt. Ltd.), Manganese acetate tetrahydrate (99%, SRL Pvt. Ltd), Potassium chloride (99.5%, SRL Pvt. Ltd), Zinc sulfate heptahydrate (99%, Alfa Aesar), Zinc chloride (98%, Sigma Aldrich), and Zinc acetate dihydrate (97%, Alfa Aesar). All the chemicals were used directly without any further purification. The electrolytic solutions were prepared by dissolving zinc and manganese based precursors in distilled water and used as anolyte (50 mL) and catholyte (50 mL) respectively. In addition to that supporting electrolyte was used such as KCl and NaCl. The role of the supporting electrolyte is to increase the ionic conductivity.

### Flow Cell Assembly and Working Principle

The schematic representation of the working principle of the Zn–Mn hybrid RFB system is depicted in Figure 1.

The flow cell setup includes a graphite composite plate grooved into 1 mm depth at an area of  $5 \text{ cm} \times 5 \text{ cm}$  on the surface of the plate. The interconnected porous flow through commercial GFA Rayon felts (SGL Carbon, SIGRACELL®, Germany) of size  $5 \text{ cm} \times 5 \text{ cm}$

( $25 \text{ cm}^2$ ) were used as an active electrode in both cathode and anode compartments. The main advantages of using the GFA electrodes are high conductivity, high surface area, cost-effective, non-toxic, and highly chemical resistant. The catholyte (50 mL) and anolyte (50 mL) solution were prepared and stored in separate tanks which were constantly pumped into the cell with the flow rate of  $30 \text{ mL min}^{-1}$  using a peristaltic pump. The flow cell performance of the Zn–Mn flow cell at various electrolyte conditions was studied in this case. The detailed combinations of various electrolytes composition investigated in the present investigation are shown in Figure 2. The gold coated copper current collector is placed behind the graphite bipolar plates which allow the electron transport to the external circuits during the GCD process. Finally, the endplate with the size of  $10 \text{ cm} \times 10 \text{ cm}$  and thickness of 2.5 cm is made up of stainless steel and it has holes at each corner where screws are placed in it to compress the cell compartment that is placed behind the current collectors on both sides. The cathode and anode compartments were separated by a microporous separator (Thickness: 1 mm, DRA-U250F212B, Daramic membrane).

### Pore-Filled Membrane Preparation

Firstly, the PAN (0.25 g) is dissolved in the 10 mL of N-methyl-2-pyrrolidone (NMP) and the solution was allowed to constant stirring until get a complete dissolution. The Daramic membrane of  $6 \text{ cm} \times 6 \text{ cm}$  was immersed in the PAN solution for about 20 min and then the film was dried at  $60^\circ\text{C}$  overnight. The PAN coated Daramic membrane was used in the flow cell studies.

### Permeability of Manganese ( $\text{Mn}^{2+}$ ) Ions

The manganese ion permeability through the Daramic membrane was explored by the following method. The positive and negative compartment of the flow cell was divided by the Daramic membrane. The positive tank comprises of 2 M  $\text{MnSO}_4$  and the negative tank comprises of distilled water which were allowed to circulate into the flow cell at  $30 \text{ mL min}^{-1}$  without any load. The effective area of the separator used in this study was  $25 \text{ cm}^2$ . Then, 2 mL of the water was taken from the tank at constant time interval of 1 h to analyze the presence of  $\text{Mn}^{2+}$  ions in water. The concentration of  $\text{Mn}^{2+}$  ions was measured by the UV-Vis spectrometer in ambient temperature. The  $\text{Mn}^{2+}$  ion permeability was calculated by the following equation [Eq. (4)]:

$$P = V \times T / A (C_0 - C_M(t)) \frac{dC_M(t)}{dt} \quad (4)$$

Where  $P$  – permeability,  $V$  – volume of the tank,  $T$  – thickness of the membrane,  $A$  – area of the membrane,  $C_0$  – concentration of  $\text{Mn}^{2+}$  ions, and  $C_M(t)$  –  $\text{Mn}^{2+}$  ion concentration in water as a function of time.

### Electrochemical Characterization

Cyclic voltammetry (CV) was performed to determine the redox reaction of the catholyte at a given potential window using the Solartron analytical cell test system. The GCD profile of the flow cell was recorded at different current densities ranging from 10 to  $40 \text{ mA cm}^{-2}$  using Scribner 857 redox flow cell test system instrument (USA).

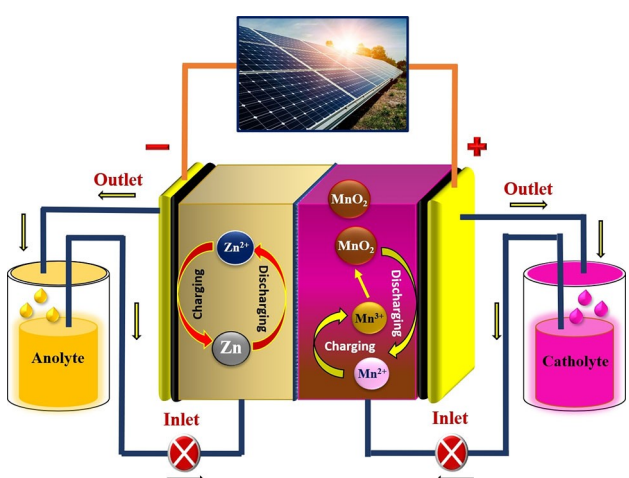


Figure 1. Schematic representation of the working principle of the Zn–Mn HRFB.

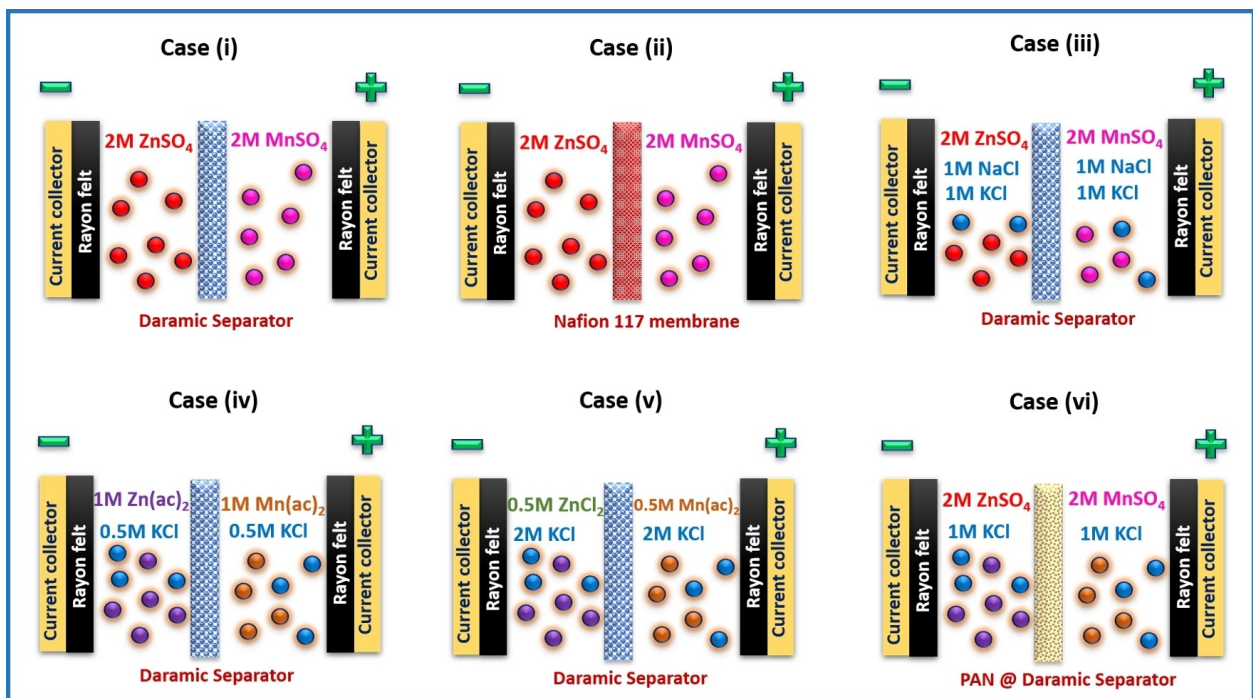
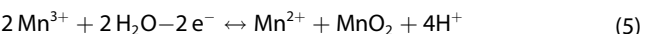


Figure 2. Schematic representation of the electrolyte composition strategy for zinc–manganese hybrid redox flow battery.

## 2. Results and Discussion

With an aim to understand the electrochemical activity of the catholyte, cyclic voltammograms (CVs) measurements were carried out for the given electrolyte composition of 0.05 M  $\text{MnSO}_4 \cdot \text{H}_2\text{O} + 1 \text{ M KCl}$  and 0.05 M  $\text{Mn}(\text{ac})_2 + 1 \text{ M KCl}$  in the potential range between 0 to 1.6 V vs Ag/AgCl. From Figure 3a, it is observed that during the forward scan, two anodic peaks were observed at 1.04 and 1.31 V vs Ag/AgCl. It corresponds to the oxidation of  $\text{Mn}^{2+}$  to  $\text{MnO}_2$  with an intermediate of  $\text{Mn}^{3+}$ . While at the reverse scan two cathodic peaks were observed at 1.16 and 0.82 V which is due to  $\text{MnO}_2$  to  $\text{Mn}^{2+}$  conversions.<sup>[37–39]</sup>

During the reaction progress,  $\text{MnO}_2$  is formed which then subsequently converted into  $\text{Mn}^{2+}$  the mechanism behind is a simple disproportionation reaction of  $\text{Mn}^{3+}$  in an aqueous solution which is described as follows [Eq. (5)]:



On the other hand,  $\text{Mn}(\text{ac})_2$  shows only one anodic peak observed at 0.80 V and one cathodic peak at 0.43 V vs Ag/AgCl, respectively. It is attributed due to the substantial oxidative conversion of  $\text{Mn}(\text{ac})_2$  to  $\text{MnO}_2$ . It shows better quasi reversibility with minimum peak separation of 0.37 V (Figure 3b). The

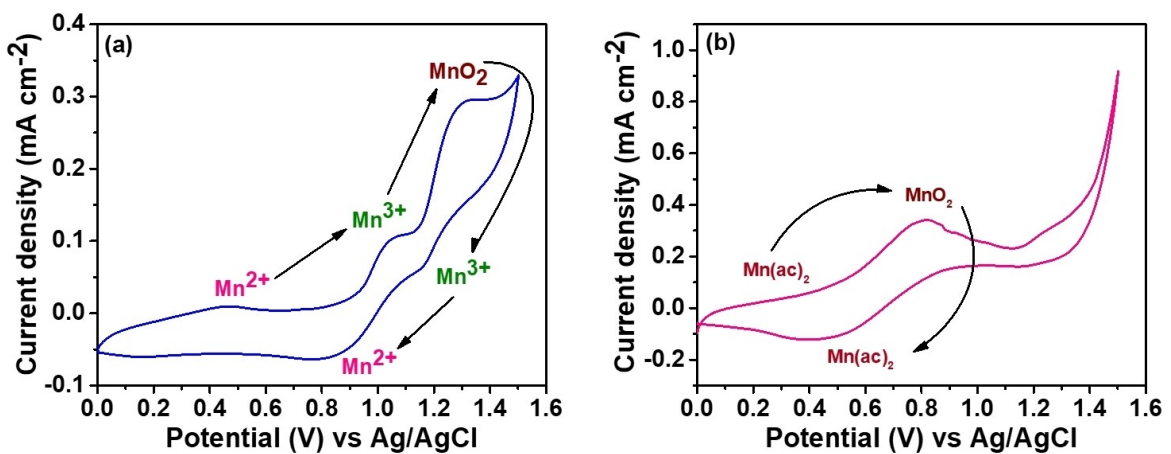


Figure 3. Cyclic voltammetry profile of the  $\text{MnSO}_4$  and  $\text{Mn}(\text{ac})_2$  recorded at a scan rate of  $16 \text{ mVs}^{-1}$  on a platinum rod a)  $0.05 \text{ M MnSO}_4 + 1 \text{ M KCl}$  and b)  $0.05 \text{ M Mn}(\text{ac})_2 + 1 \text{ M KCl}$

better reversibility is attributed due to the coordinating effect of acetate ion.<sup>[32]</sup> To ensure redox behaviour at different scan rate was also studied and the obtained CV curves are shown in Figure S1a and S1b.

## 2.1. Electrolyte Optimization Strategy

In order to understand the influence of different electrolytes compositions on the flow cells performance, various combination of electrolytes combinations is studied. The investigation of the electrolyte composition strategy provides a significant result which helps us to identify a better electrolyte composition for a high-performance Zn–Mn hybrid flow battery. The 3<sup>rd</sup> cycle GCD performance recorded at different electrolyte conditions at 10 mA cm<sup>-2</sup> of flow cell is shown in Figure 4a and the corresponding voltage drops observed at each conditions of the flow cell are shown Figure 4b. In case (i) 2 M ZnSO<sub>4</sub> and 2 M MnSO<sub>4</sub> are used as anolyte and catholyte, respectively, with Daramic membrane as a separator. In this case, we observed that the flow cell exhibits a greater discharge plateau voltage of 1.83 V with an IR drop of 236 mV (Figure 4a and 4b). However, the flow cell shows continuous capacity fade in the subsequent charge-discharge cycles due to severe crossover of the electrolyte even at a current density of 20 mA cm<sup>-2</sup>. In order to confirm this ion crossover, ion permeability was observed. Figure S2 displays the permeability of Mn<sup>2+</sup> ion through the Daramic membrane in a given condition. The Daramic membrane showed a gradual increase of Mn<sup>2+</sup> ion permeability from positive to negative compartment over the period of time. The Daramic membrane exhibits a Mn<sup>2+</sup> permeability of  $21.6 \times 10^{-9}$  cm<sup>2</sup> min<sup>-1</sup> in the 3hr duration. This is well correlated with the GCD characteristic observed in case (i).

In case (ii) we adopted a Nafion-117 membrane as a separator in the same electrolyte composition to study the effect of the ion crossover. The charging voltage suddenly reached 2.21 V and the discharge time gets reduced, which is shown in Figure S3a. Thus, during overcharging the catholyte color changes from pale pink to dark brown which indicates

the formation of MnO<sub>2</sub> (Mn<sup>4+</sup>). Due to the poor solubility of MnO<sub>2</sub> particles in an aqueous medium, it is deposited on the electrode surface of the felt electrode. Further, the voltage drop was also increased drastically to 460 mV altogether limits the performance of the flow cell in real-time applications. Hence, the use of Nafion-117 membrane for subsequent optimization cases is avoided. In case (iii), we employed two different supporting electrolytes such as KCl and NaCl in the same electrolyte composition with a Daramic separator. This attempt exhibits improved flow cell performance with an average charging voltage of 2.09 V. It shows a larger discharge voltage of 1.92 V, with the very minimum voltage drop of 138 mV and there is a substantial improvement in the discharging time in the flow cell was also observed. Moreover, this strategic mode reaches a high potential of 2.71 V when operating at 40 mA cm<sup>-2</sup> current density, as a result, there is a severe deposition of MnO<sub>2</sub> on the electrode surface. It further limits the flow cell performance. In case (iv), we used Zn(ac)<sub>2</sub> and Mn(ac)<sub>2</sub> as anolyte and catholyte, respectively with 0.5 M KCl as a supporting electrolyte. The charging voltage is limited to 1.68 V due to poor zinc plating and stripping process. The acetate-based precursors have a greater coordinating ability towards metal ions, so it affects the plating and stripping process of zinc due to which the potential is not reached 1.8 V and above which is depicted in Figure S3b. This could be confirmed by using ZnCl<sub>2</sub> as anolyte (case v). In case (v), the charging voltage reaches 1.76 V slightly higher than case (iv) but still lower than 1.8 V which is shown in Figure S3c. It is mainly due to the acetate precursor in the catholyte. Thus, acetate-based zinc and manganese precursors are not well suitable for flow battery performance. Hence in the final case (case vi), we went for sulfate-based precursors of zinc and manganese with polyacrylonitrile (PAN) fabricated Daramic membrane as a separator for Zn–Mn flow cell studies. The PAN fabricated Daramic membrane controls the crossover of the electrolyte to a maximum extent and withstands wider operating current densities such as 10, 20, 30, and 40 mA cm<sup>-2</sup>, respectively. The PAN fabricated Daramic membrane exhibits enhanced performance with an average charging voltage of

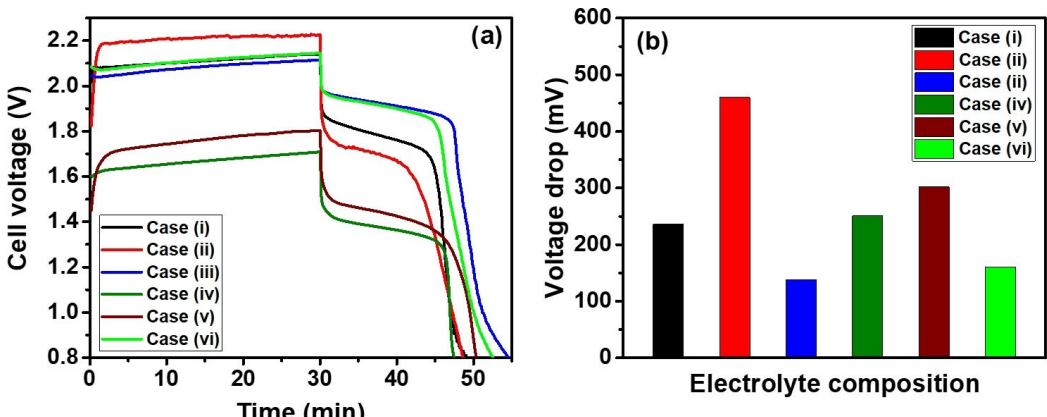


Figure 4. a) Galvanostatic charge-discharge (GCD) profile for different electrolyte composition recorded at a current density of 20 mA cm<sup>-2</sup> and b) electrolyte composition vs voltage drop profile of the flow cell tested at various conditions.

2.11 V, and more interestingly it discharges at a higher voltage of 1.92 V with a very minimum voltage drop of 160 mV at  $20 \text{ mA cm}^{-2}$ . Thus, case (vi) is chosen as the best-optimized electrolyte composition for Zn–Mn hybrid flow battery applications.

## 2.2. Galvanostatic Charge–Discharge Studies

The GCD profile of the Zn–Mn flow cell was tested at various current densities. Accordingly, Figure 5a shows the charge-discharge curves recorded in 2 M  $\text{ZnSO}_4$  as anolyte and 2 M  $\text{MnSO}_4$  as catholyte whereas 1 M KCl is used as a supporting electrolyte. The Daramic membrane coated (pore filled) with PAN was employed as a separator in this case. The voltage drop observed here are 140, 250, 380, and 620 mV at 10, 20, 30, and  $40 \text{ mA cm}^{-2}$ , respectively. The gradual increase in voltage drop was noticed on increasing the current density and it is mainly due to the polarization on the electrode surface which is a usual phenomenon in any electrochemical system. Besides that, while discharging, the obtained improved linear plateau indicated the improved ohmic loss of the system. The improved ohmic loss enhances the ionic transfer at the electrode–electrolyte interface. Further, the cell performance was estimated by obtaining the efficiency values of the system. The coulombic efficiency (CE), voltage efficiency (VE), and energy efficiency (EE) are the significant parameters for evaluating the flow battery performance. The detailed formula for calculating CE, VE, and EE is given here: Voltage efficiency (VE%) = avg. discharge voltage/avg. charge voltage × 100; Coulombic efficiency (CE%) = discharge capacity/charge capacity × 100; Energy efficiency (EE%) = (VE × CE)/100.

The flow cell exhibits as high as columbic efficiency of 83% at  $20 \text{ mA cm}^{-2}$  and the corresponding VE and EE are 86.2% and 75.6%, respectively, as shown in Figure 5b. The efficiency values obtained at various conditions of the flow cell was given in Figure S4. With this designed configuration, the Zn–Mn flow cell with PAN anchored Daramic membrane delivered the

maximum energy density of  $12.31 \text{ Wh L}^{-1}$  at  $34.19 \text{ W L}^{-1}$  at a current density of  $40 \text{ mA cm}^{-2}$ .

To understand factors that influence the cycling stability of the system the cell was tested at various current densities (10, 20, 30, and  $40 \text{ mA cm}^{-2}$ ). It was noted that the increase of current density slightly increases the cell charging voltage due to high polarization. The cell shows maximum efficiencies at 10 and  $20 \text{ mA cm}^{-2}$  and the GCD profile observed for the first five cycles at different current densities are shown in Figure 6(a–d). The energy density estimated at different current density is given in Table S1.

The efficiency performance was obtained by testing the flow cells at different current densities. Accordingly, the enhanced performance is mainly attributed to the facile conversion of  $\text{Mn}^{2+} \leftrightarrow \text{MnO}_2$  redox couple and absence of crossover of the electrolyte. For comparison, the FESEM image of pristine Daramic membrane is shown in Figure 7a clearly indicating the existence of pores. The approximate pore size distribution in the pristine Daramic membrane is around 325 nm ( $\pm 5 \text{ nm}$ ). The presence of micropores ameliorates the ion crossover over the long cycling. The PAN polymer coated Daramic membrane greatly inhibits the ion crossover wherein PAN moieties are successfully blocked the pores in the Daramic membrane as seen in FESEM image (Figure 7b). The enhanced performance is evidenced from the prolonged cycle testing of flow cell. The PAN modified Daramic membrane shows an excellent stability over 100 GCD cycles. Thus, the adopted flow cell strategic condition exhibits stable performance up to  $40 \text{ mA cm}^{-2}$  current density. However, a prolonged cycling process leads to the deposition of residual  $\text{MnO}_2$  on the surface of rayon felt which was confirmed by FESEM surface imaging and also EDX spectrum (Figure S5a–b and S5c). As a result, there is a substantial rise in voltage was observed as shown in Figure 8a. It is observed that accumulated  $\text{MnO}_2$  also contributes for increasing the internal resistance of the flow cell which is evidenced from the high frequency resistance (HFR) profile Figure 9.

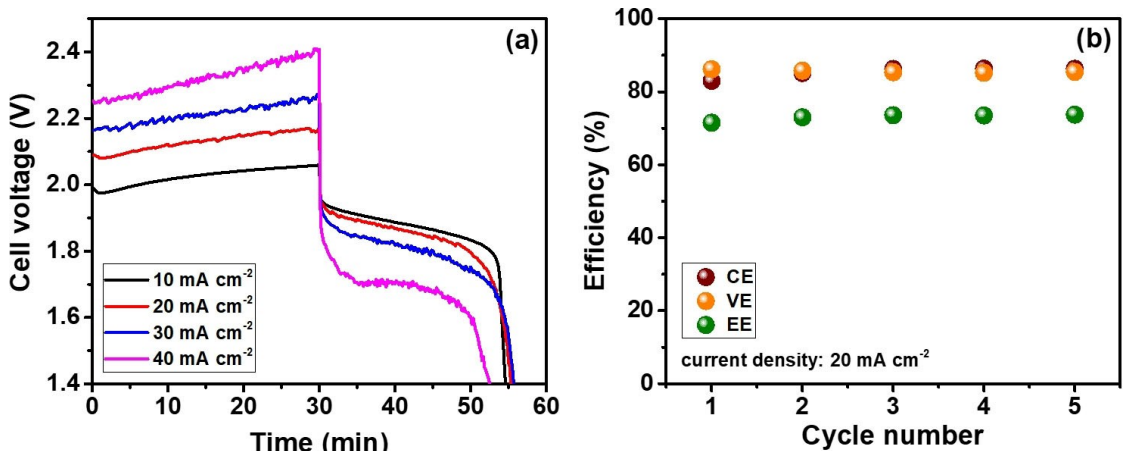


Figure 5. a) GCD curves at different current densities and b) efficiencies of Zn–Mn flow cell system.

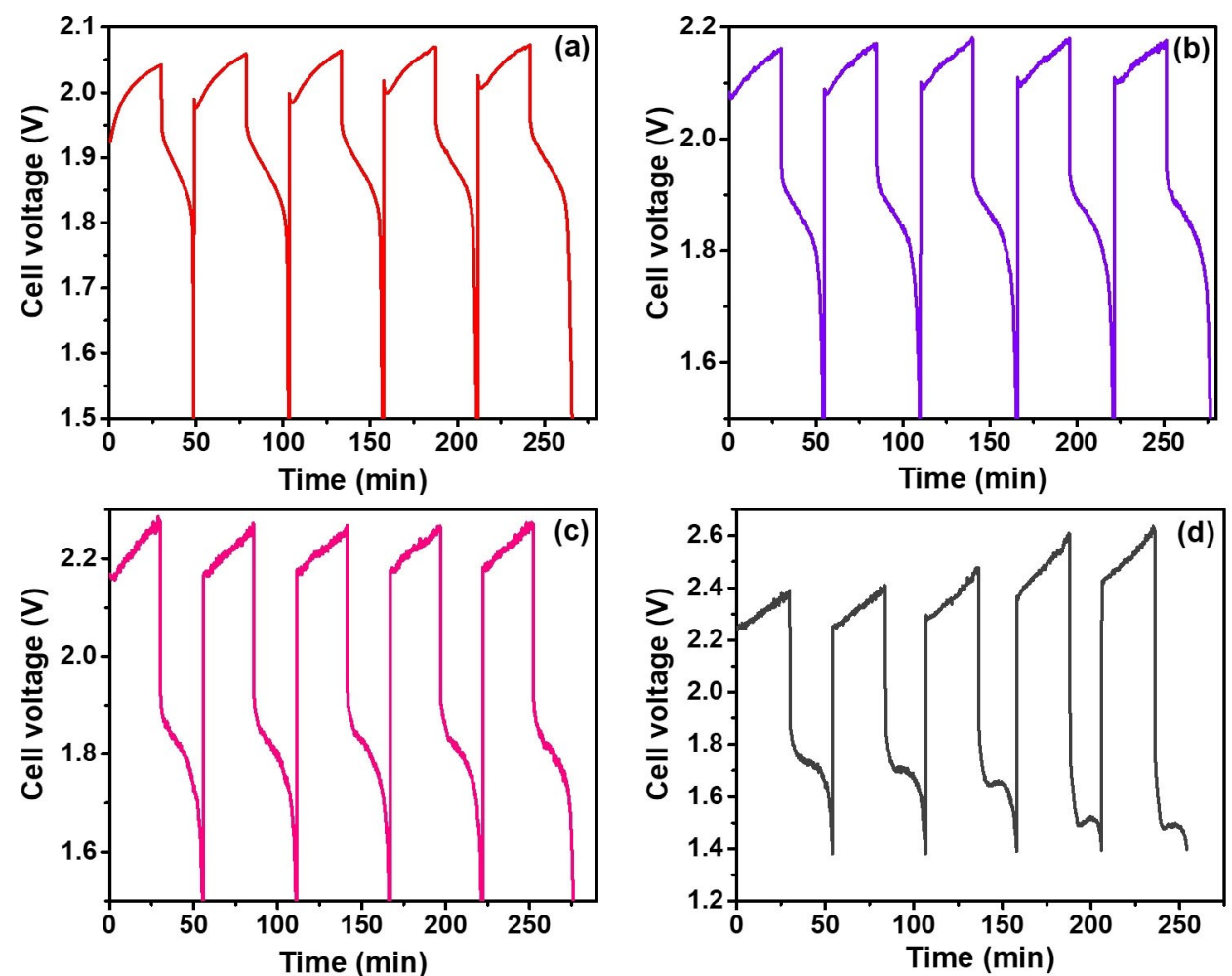


Figure 6. GCD profile recorded at a) 10, b) 20, c) 30 and d) 40  $\text{mA cm}^{-2}$  current density.

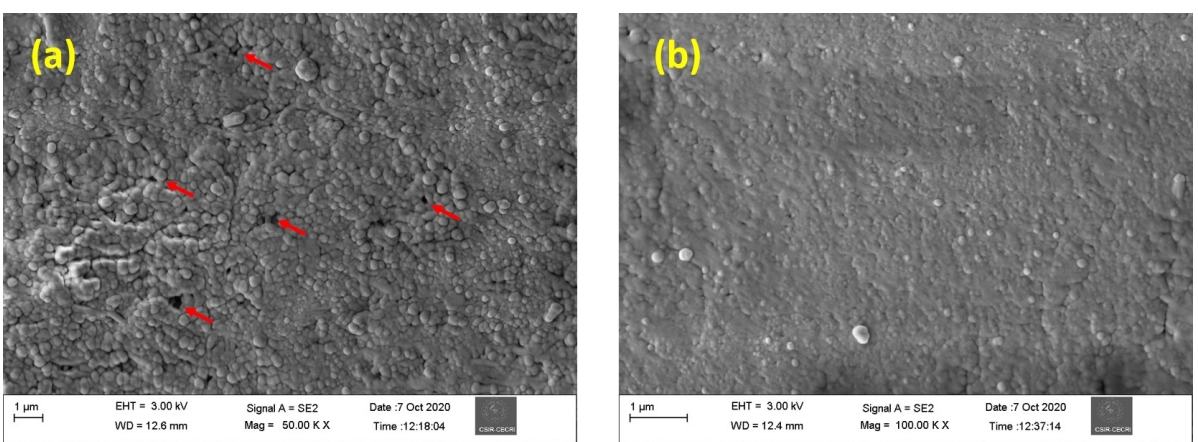
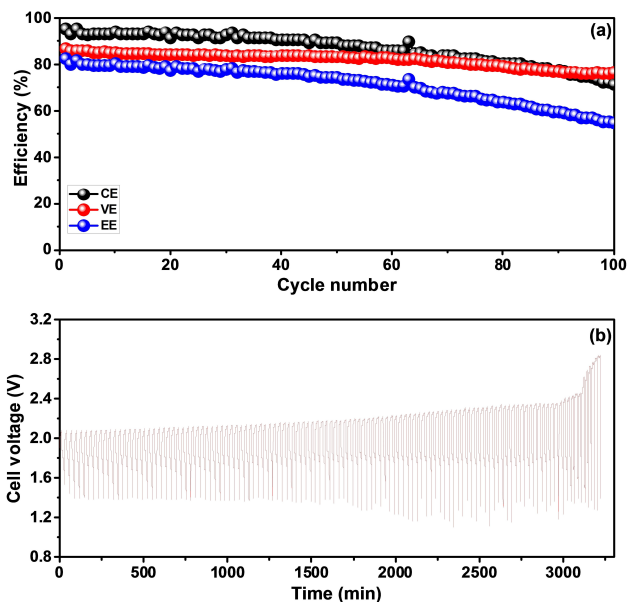


Figure 7. FESEM imaging of a) Daramic membrane and b) PAN fabricated Daramic membrane.

### 2.3. Cycling Performance Analysis

The durability of the PAN coated Daramic membrane was examined by a long cycling tested at a current density of  $20 \text{ mA cm}^{-2}$  for 15 min each charge and discharge time.

Interestingly, the cell exhibits a steady performance over up to 100 cycles with the VE of 80% as shown in Figure 8b. The excellent durability and stability of the PAN anchored Daramic membrane was reflected in the CE (87%) and EE (72%) over an average of 100 GCD cycles (Figure 8b). Moreover, the electro-



**Figure 8.** Flow cell performance tested at  $20 \text{ mA cm}^{-2}$ : a) CE, VE and EE%; b) GCD cycle life profile of Zn–Mn system.

lyte volume was not changed drastically and only 2 mL difference is noted from the initial volume of the electrolyte (50 mL) while PAN coated membrane. This also the best indication for stability of the PAN anchored Daramic membrane. However, there is a slight increase in charging voltage noticed after 90<sup>th</sup> cycles, this is due to the accumulation of residual MnO<sub>2</sub> particles on the felt. During consecutive charge discharge cycles, the MnO<sub>2</sub> gets plated in the direction towards the separator and gets deposited over the separator. It is evidenced from the FESEM images as shown in Figure S5a at the 100<sup>th</sup> cycle (post analyzed electrode). The presence of residual MnO<sub>2</sub> particles eventually increases the flow cell resistance of approximately 850 mΩ at the last 10 cycles as shown in Figure 9a.

Figure 9b indicates the impedance spectra of the given active electrode in different electrolyte conditions. It was observed that the sample both the electrolyte conditions showed similar trend (i.e. incomplete behavior of the semi-circle) at the tested frequency conditions. The enlarged view clearly showed the less solution resistance for acetate based precursor electrolyte (7.1 Ohm) when compared with the sulphate precursor based sample (9.9 Ohm). In both cases, the linear spike inclined at an angle around 45° indicates the strong diffusion of the redox process at the electrode/electrolyte interface. However, there was huge variation observed in charge transfer resistance ( $R_{ct}$ ) between the two samples. The GF electrode at 0.05 M Mn(ac)<sub>2</sub> + 1 M KCl and 0.05 M MnSO<sub>4</sub> + 1 M KCl showed a  $R_{ct}$  value of ~25.5 Ohm and ~4.7 kOhm, respectively. This huge variation in the  $R_{ct}$  value also reflected in the flow cell performance.

The Zn–Mn hybrid flow battery is a proficient candidature for futuristic large scale stationary energy storage applications due to the existence of remarkable properties such as high cell voltage, corrosive free, non-toxic, eco-friendly, and presence of various oxidation states of manganese. Though the Zn–Mn redox couple exhibits better flow cell performance, still it is encountered by critical issues which are needed to be overcome. The various intrinsic issues are: (i) the ununiform deposition of MnO<sub>2</sub> on the carbon felt severely affect the areal capacity. (ii) the poor reversibility of MnO<sub>2</sub> on the electrode subsequently alleviates the charging voltage of the flow cell; hence, it limits the operational current density lower than  $40 \text{ mA cm}^{-2}$ ; (iii) the insoluble tendency of MnO<sub>2</sub> causes various issues such as pressure drop, flow field blocking, and reduced mass transport; (iv) the structural collapse of MnO<sub>2</sub> during GCD also affects the flow cell performance; (v) the highly unstable oxidation state of Mn<sup>3+</sup> in the aqueous medium. Thus, more research is to be concerned to realize the commercialization of the Zn–Mn flow battery.

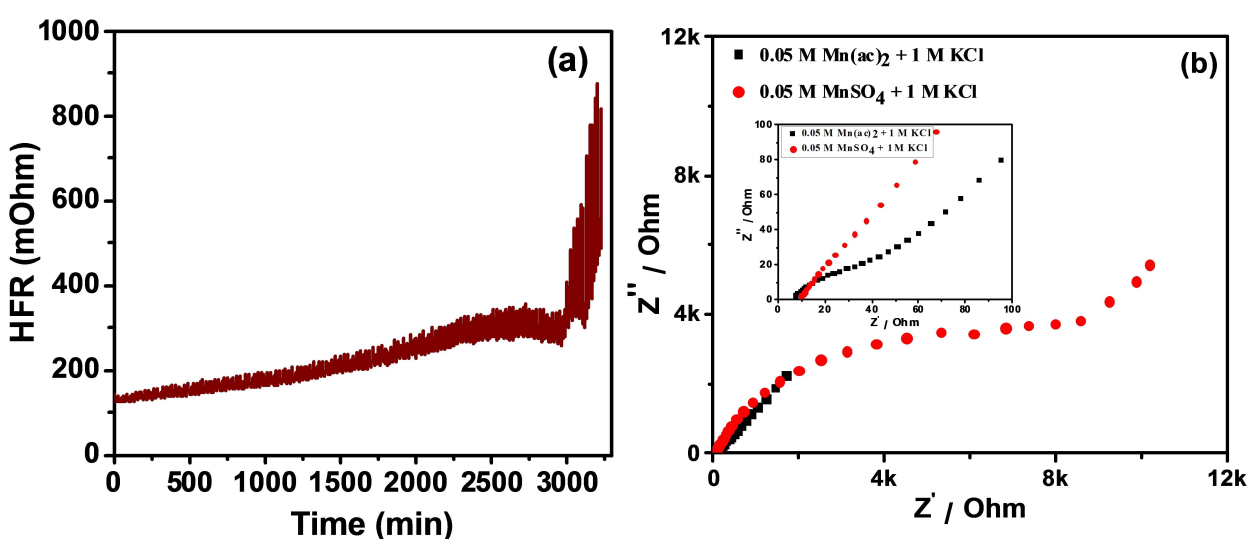


**Figure 9.** HFR profile obtained at  $20 \text{ mA cm}^{-2}$  current density over 100 GCD cycles.

### 3. Conclusions

In summary, the PAN moieties are successfully anchored on the Daramic membrane by the casting method. It shows excellent performance with 80% voltage efficiency over 100 cycles without fade in performance. It indicates that simple, low cost PAN is a well suitable polymer for hampering ion crossover in the flow cell. Surprisingly, the sulfate-based precursors exhibit a greater discharge voltage of 1.91 V. The as configured Zn–Mn flow cell delivered the energy density of  $12.31 \text{ Wh L}^{-1}$  at  $34.19 \text{ WL}^{-1}$  in  $40 \text{ mA cm}^{-2}$  current density. Thus, the Zn–Mn system is considered as one of the reliable cost effective candidature for large scale storage of electricity in near future.

### Acknowledgements

M. U. acknowledges the financial support received from the DST-SERB through Ramanujan Fellowship (DST-SERB, SB/S2/RJN-082/2016).

### Conflict of Interest

The authors declare no conflict of interest.

**Keywords:** aqueous zinc–manganese flow batteries • sulfate-based electrolytes • high discharge voltage • Daramic membrane, electrolytes

- [1] L. Zhang, H. Zhang, Q. Lai, X. Li, Y. Cheng, *J. Power Sources*. **2013**, *227*, 41–47.
- [2] L. I. Minchala-Avila, J. Armijos, D. Pesántez, Y. Zhang, *Energy Procedia*. **2016**, *103*, 195–200.
- [3] M. H. Chakrabarti, S. A. Hajimolana, F. S. Mjalli, M. Saleem, I. Mustafa, *Arabian J. Sci. Eng.* **2013**, *38*, 723–739.
- [4] Y. Wang, B. Liu, Q. Li, S. Cartmell, S. Ferrara, Z. D. Deng, J. Xiao, *J. Power Sources*. **2015**, *286*, 330–345.
- [5] G. J. May, A. Davidson, B. Monahov, *J. Energy Storage*. **2018**, *15*, 145–157.
- [6] M. L. Perry, A. Z. Weber, *J. Electrochem. Soc.* **2016**, *163*, 5064–5067.
- [7] Z. Yuan, Y. Yin, C. Xie, H. Zhang, Y. Yao, X. Li, *Adv. Mater.* **2019**, *31*, 1–27.
- [8] J. Sarkar, S. Bhattacharya, *Arch. Thermodyn.* **2012**, *33*, 23–40.
- [9] M. Bartolozzi, *J. Power Sources*. **1989**, *27*, 219–234.
- [10] F. P. Documents, O. Publications, (12) United States Patent, 1 (2004).
- [11] Z. Wang, J. Parrondo, V. Ramani, *J. Electrochem. Soc.* **2017**, *164*, 372–378.
- [12] S. Suresh, M. Ulaganathan, N. Venkatesan, P. Periasamy, P. Ragupathy, *J. Energy Storage*. **2018**, *20*, 134–139.
- [13] K. Mariyappan, R. Velmurugan, B. Subramanian, P. Ragupathy, M. Ulaganathan, *J. Power Sources*. **2021**, *482*, 228912.
- [14] R. Naresh, K. Mariyappan, K. S. Archana, S. Suresh, D. Ditty, M. Ulaganathan, P. Ragupathy, *ChemElectroChem* **2019**, *6*, 5688–5697.
- [15] M. Rybachik, M. Skyllas-Kazacos, *J. Power Sources*. **1988**, *22*, 59–61.
- [16] G. M. Weng, Z. Li, G. Cong, Y. Zhou, Y. C. Lu, *Energy Environ. Sci.* **2017**, *10*, 735–741.
- [17] Y. K. Zeng, X. L. Zhou, L. An, L. Wei, T. S. Zhao, *J. Power Sources*. **2016**, *324*, 738–744.
- [18] Y. K. Zeng, T. S. Zhao, L. An, X. L. Zhou, L. Wei, *J. Power Sources*. **2015**, *300*, 438–443.
- [19] K. S. Archana, S. Suresh, P. Ragupathy, M. Ulaganathan, *Electrochim. Acta*. **2020**, *345*, 136245.
- [20] C. Tang, D. Zhou, *Electrochim. Acta*. **2012**, *65*, 179–184.
- [21] K. Gong, X. Ma, K. M. Conforti, K. J. Kuttler, J. B. Grunewald, K. L. Yeager, M. Z. Bazant, S. Gu, Y. Yan, *Energy Environ. Sci.* **2015**, *8*, 2941–2945.
- [22] M. Ulaganathan, S. Suresh, K. Mariyappan, P. Periasamy, R. Pitchai, *ACS Sustainable Chem. Eng.* **2019**, *7*, 6053–6060.
- [23] J. D. Jeon, H. S. Yang, J. Shim, H. S. Kim, J. H. Yang, *Electrochim. Acta*. **2014**, *127*, 397–402.
- [24] M. C. Wu, T. S. Zhao, L. Wei, H. R. Jiang, R. H. Zhang, *J. Power Sources*. **2018**, *384*, 232–239.
- [25] S. Suresh, T. Kesavan, Y. Munaiah, I. Arulraj, S. Dheenadayalan, P. Ragupathy, *RSC Adv.* **2014**, *4*, 37947–37953.
- [26] W. Lu, C. Xie, H. Zhang, X. Li, *ChemSusChem*. **2018**, *11*, 3996–4006.
- [27] S. Selverston, R. F. Savinell, J. S. Wainright, *J. Electrochem. Soc.* **2017**, *164*, 1069–1075.
- [28] S. Suresh, M. Ulaganathan, R. Aswathy, P. Ragupathy, *ChemElectroChem* **2018**, *5*, 3411–3418.
- [29] P. K. Leung, C. Ponce De Leon, F. C. Walsh, *Electrochim. Acta*. **2012**, *80*, 7–14.
- [30] A. Khor, P. Leung, M. R. Mohamed, C. Flox, Q. Xu, L. An, R. G. A. Wills, J. R. Morante, A. A. Shah, *Mater. Today* **2018**, *8*, 80–108.
- [31] J. Huang, Z. Guo, X. Dong, D. Bin, Y. Wang, Y. Xia, *Sci. Bull.* **2019**, *64*, 1780–1787.
- [32] C. Xie, T. Li, C. Deng, Y. Song, H. Zhang, X. Li, *Energy Environ. Sci.* **2020**, *13*, 135–143.
- [33] Y. Dong, H. Kaku, H. Miyawaki, R. Tatsumi, K. Moriuchi, T. Shigematsu, *SEI Tech. Rev.* **2017**, *69*, 35–40.
- [34] T. Hong, F. Xue, *Asia-Pacific Power Energy Eng. Conf. APPEEC* **2009**, 2–5.
- [35] L. Wei, L. Zeng, M. C. Wu, H. R. Jiang, T. S. Zhao, *J. Power Sources*. **2019**, *423*, 203–210.
- [36] W. Chen, G. Li, A. Pei, Y. Li, L. Liao, H. Wang, J. Wan, Z. Liang, G. Chen, H. Zhang, J. Wang, Y. Cui, *Nat. Energy*. **2018**, *3*, 428–435.
- [37] L. Wei, H. R. Jiang, Y. X. Ren, M. C. Wu, J. B. Xu, T. S. Zhao, *J. Power Sources*. **2019**, *437*, 226918.
- [38] D. Reynard, S. Maye, P. Peljo, V. Chanda, H. H. Girault, S. Gentil, *Chem. A Eur. J.* **2020**, *26*, 7250–7257.
- [39] A. E. S. Sleightholme, A. A. Shinkle, Q. Liu, Y. Li, C. W. Monroe, L. T. Thompson, *J. Power Sources*. **2011**, *196*, 5742–5745.

Manuscript received: March 18, 2021

Revised manuscript received: May 7, 2021

Accepted manuscript online: May 12, 2021

Version of record online: June 18, 2021